Polymer Bulletin (2024) 81:3229–3255
https://doi.org/10.1007/s00289-023-04850-1

ORIGINAL PAPER

PVDF-based $(V_2O_5)_{x.}$ $(Mn_{0.4}Fe_{2.6}O_4)_{(2-x)}$, $x = [0.2, 0.4, 0.6, 0.8, \text{and } 1]$ nanocomposites for tailoring the optical and nonlinear optical properties of PVDF

Rania Ramadan[1] · M. K. Ahmed[2,3] · Mai M. El-Masry[4]

Received: 3 December 2022 / Revised: 30 April 2023 / Accepted: 5 May 2023 /
Published online: 2 June 2023

Abstract

Nanocomposites comprising $(V_2O_5)_{x.}$ $(Mn_{0.4}Fe_{2.6}O_4)_{(2-x)}$, where $x = [0.2, 0.4, 0.6, 0.8, \text{and } 1]$, were successfully synthesized by milling each single phase of V_2O_5 and $Mn_{0.4}Fe_{2.6}O_4$ nanostructured samples. We studied the structure and morphology of the prepared samples through X-ray diffraction and scanning electron microscopy. UV–Vis. spectrum analysis was used to study the optical characteristics. As an attempt to improve the optical and nonlinear optical properties of the PVDF blend, the prepared nanocomposites were used as nanofillers for the poly (vinylidene fluoride) (PVDF) polymer. Optical and nonlinear optical properties of the PVDF polymer were tuned using $(V_2O_5)_{x.}$ $(Mn_{0.4}Fe_{2.6}O_4)_{(2-x)}$, where $x = [0.2, 0.4, 0.6, 0.8, \text{and } 1]$ nanocomposite. The obtained results showed a tunable spectrum, absorption, refractive index, and dielectric constant at wavelengths ranging from 200 to 800 nm. However, the results showed that the $(V_2O_5)_{0.6.}$ $(Mn_{0.4}Fe_{2.6}O_4)_{1.4}$, sample was the best for obtaining the lowest transmittance percentage and bandgap energy. The nonlinear optical properties and Kerr effect (quadratic electro-optic effect) showed a significant response, which can be tuned in the range from 200 to 1200 nm of wavelength using the investigated samples. Finally, incorporating $(V_2O_5)_{x.}$ $(Mn_{0.4}Fe_{2.6}O_4)_{(2-x)}$, where $x = [0.2, 0.4, 0.6, 0.8, \text{and } 1]$, nanoparticles in the PVDF polymer improved the hydrophilic behavior of the PVDF films. This study suggests a promising nanocomposite material for tunable optoelectronics and useful polymer membranes.

Keywords Dielectric properties · Nonlinear optical effects · Optoelectronic · Polymer

Extended author information available on the last page of the article

Introduction

Nanomaterials have transformed various technological applications, from solar cells and lasers to electronic devices, owing to their unique magnetic, optical, mechanical, and electrical characteristics [1, 2]. One such nanomaterial that has garnered significant interest is magnetite, which exhibits high magnetic and electric properties. The crystal structure of magnetite is characterized by a closed-packed cubic arrangement, as reported in previous studies [3–7]. The crystal structure of magnetite exhibits both octahedral and tetrahedral interstitial positions and has high magnetic and electric characteristics [8]. The process of doping magnetite has been identified as a highly effective technique for enhancing its magnetic properties. In comparison to the typical magnetic properties exhibited by undoped magnetite, the saturation magnetization of magnetite doped with Mn^{2+} is enhanced by approximately 50% [9].

The magnetization properties of magnetite are influenced by the distribution of cations and the V^{5+} content [10, 11]. V_2O_5 has garnered interest because of its extraordinary dielectric properties, such as improved optical conductivity and low sintering temperature. Its transition from a semiconductor to a metal phase happens around a critical temperature of 257 °C. This phase change not only alters the crystal structure of V_2O_5 but also significantly impacts its electrical and optical properties. With its potential for use in luminescence and microwave technology, vanadium pentoxide is indeed an attractive option as discussed in reference [12]. By combining distinct phases of Mn-doped magnetite and vanadium oxide, researchers expect to create new compounds that have optimal magnetic, electrical, optical, and nonlinear optical properties. Even though ceramic materials exhibit strong dielectric characteristics, their workability is inhibited by their fracture strength and brittleness. On the contrary, polymers exhibit high tensile strength and flexibility but have a lower dielectric constant. To exhibit the energy density of high performance, flexible composites, researchers have found that incorporating inorganic nanoparticles into polymer matrices is an effective approach [9]. The integration of polymers and nanomaterials has been found to enhance the practical applications of nanomaterials and ameliorate their properties [13]. Various polymers have been utilized as effective membranes and have been incorporated with inorganic materials to enhance their optical characteristics. Polyvinyl alcohol (PVA), polyvinylpyrrolidone (PVP), a blend of PVA/PVP, and a polymeric combination of polyvinyl alcohol, carboxymethyl cellulose, and polyethylene glycol have been identified as promising materials for optoelectronic applications [14, 15]. The utilization of conducting polymers in electronics has been a subject of interest. Among these polymers, Poly (Vinylidene Fluoride) (PVDF) has been found to be particularly advantageous due to its highly electroactive properties. Additionally, PVDF is flexible and can be conveniently processed into sheets of the desired shape and size. The polymer capacitor dielectric installation is suitable for high-energy–density storage applications due to its high dielectric constant, low dissipation factor, and resistance to dielectric breakdown [8]. The amount of the filler nanoparticles present in the PVDF

matrix has a significant impact on the crystallite size, crystallization kinetics, crystal morphology, and matrix crystallinity [16]. Various published studies have investigated the incorporation of different nanomaterials into PVDF polymer and analyzed their impact on the physical properties of the polymer. Ghazali and colleagues conducted a study to explore the impact of varying quantities of functionalized nano-Al_2O_3 on the properties of polyvinylidene fluoride (PVDF) [17]. The researchers have achieved success in the development of a super-amphiphilic coating that exhibits self-cleansing, anti-icing, and anti-corrosion properties. The investigation of the correlation between the optical properties of nanocomposites and the concentration of ZnO was conducted by Indolia et al. As reported in their study, the optical bandgap revealed a value of 4.95 eV when the ZnO content was 9 wt% [18]. Shaltout et al. [19] proposed a straightforward casting method for the preparation of polyvinylidene fluoride (PVDF) polymer doped with varying concentrations of molybdenum disulfide (MoS_2) nanosheets. The study investigates the compositional, structural, and optical properties of MoS_2 nanosheets that are doped in PVDF at different concentrations, ranging from 0.1 to 3 percent. The concentration of MoS_2 has been found to have a significant impact on the optical bandgap, with a decrease observed from 5.72 to 1.83 eV as the concentration of MoS2 increases. The study presented by Sylvie Ribeiro and colleagues investigates the impact of silicone nanoparticles on the physicochemical characteristics of polyvinylidene fluoride (PVDF). The incorporation of silicone nanoparticles has been found to enhance the water surface angle by up to 34% in comparison to pure PVDF, as reported in reference [20]. Nanocomposites have been developed by Gaabour et al. [21] through blending polyvinylidene fluoride (PVDF) polymers with methyl methacrylate (PMMA) doped with varying concentrations of Fe_3O_4 nanoparticles. The authors found that the direct bandgap values obtained from the UV–Vis investigation were decreased to 3.01 eV. Certain findings indicate an enhancement in the properties of polyvinylidene fluoride (PVDF) through the incorporation of magnetic ferrite nanoparticles, such as Fe_3O_4 [22], $CoFe_2O_4$ [23] and Manganese-doped magnetite [24]. Manganese-doped magnetite is a highly desirable spinel ferrite due to its exceptional chemical and thermal stability. Its versatile applications in storage devices, spintronics, and power electronics devices make it an attractive material for research and development [24].

In the present work, we will study the synthesis of PVDF-based $(V_2O_5)_x.(Mn_{0.4}Fe_{2.6}O_4)_{(2-x)}$ nanocomposites, with x=[0.2, 0.4, 0.6, 0.8, and 1], has the potential to tailor the optical and nonlinear optical properties of PVDF by integrating distinct phases of Mn-doped magnetite and vanadium oxide. This integration can yield novel compounds possessing desired optical characteristics while overcoming the limitations of ceramic materials and enhancing the practical applications of polymers when combined with inorganic nanoparticles.

Materials and methods

Analytical grade of ammonium metavanadate, oxalic acid dihydrate, manganese chloride tetrahydrate ($MnCl_2{\cdot}4H_2O$), ferrous chloride tetrahydrate ($FeCl_2{\cdot}4H_2O$), nitric acid, ferric chloride hexahydrate ($FeCl_3{\cdot}6H_2O$), ammonium chloride and sodium metavanadate was used with purity (98%) and were bought from Sigma-Aldrich Company.

V_2O_5 was prepared by dissolving sodium metavanadate in deionized water. Then ammonium chloride (1.2 g) was combined drop by drop over the solution, after that the temperature was lifted to 80 °C. Finally, the pH value was adjusted to 8. The resulting product was calcined for 4 h. at 600 °C. $Mn_{0.6}Fe_{2.4}O_4$ was prepared by the co-precipitation technique as mentioned in previous work [24]. $(V_2O_5)_x$ $(Mn_{0.4}Fe_{2.6}O_4)_{(2-x)}$, $x = [0.2, 0.4, 0.6, 0.8,$ and $1]$ was synthesized by grinding the desired amount of single phase V_2O_5 and $Mn_{0.4}$ $Fe_{2.6}O_4$ nanostructured samples for 2 h. Nanocomposite films were prepared by using two solutions. First, each sample's 10 g of PVDF powder was dissolved in 20 [ml] of *N*-Methyl-2-pyrrolidone (NMP), a polar aprotic solvent. Then stir at room temperature until the mixture was clear. First, each sample's 10 g of PVDF powder was dissolved in 20 [ml] of *N*-Methyl-2-pyrrolidone (NMP), a polar aprotic solvent. Then stirred at room temperature until the mixture was clear. Another suspension was made and sonicated using 0.05 gm of $(V_2O_5)_x$ $(Mn_{0.4}Fe_{2.6}O_4)_{(2-x)}$, $x = [0.2, 0.4, 0.6, 0.8$ and $1]$. The PVDF solution was then mixed with the nanoparticle suspension and sonicated for one hour. Finally, transfer the resulting mixture to a clean Petri dish while maintaining a heating plate temperature of 80 °C. The obtained film thicknesses for $(V_2O_5)_x$ $(Mn_{0.4}Fe_{2.6}O_4)_{(2-x)}$, $x = [0.2, 0.4, 0.6, 0.8,$ and $1]$ correspondingly were (0.14, 0.45, 0.15, 0.12, and 0.12 mm).

Gotten tests were interpreted by XRD (Analytical x, Pertpro, Cu kα1 target, $\lambda = 1.5404$ Å, 45 kV, 40 mA, Netherlands). The XRD was utilized in the range 2θ from 10° to 70°. A field emission scanning electron microscope FESEM (FE-SEM, QUANTA-FEG250, Netherlands, operating voltage around 20–30 kV) was used to examine the morphologies under investigation. (UV–Vis.) spectroscopic analysis was carried out for all investigated composites of different concentrations using (Cary 5000 UV–Vis–NIR Spectrophotometer, wavelength range from 190 to 2000 nm, version 1.12, dual beam mode).

Results and discussion

XRD

The crystal structure of the assembled nanocomposites was examined by XRD, as palpable in Fig. 1a. It would be able to see that the characteristic peaks associated with the ICDD card [04-022-8591] cubic structure of $Mn_{0.4}Fe_{2.4}O_4$ can be found at $2\theta = 34.33°$, 63.37° and match the Miller indices of (311) and (440),

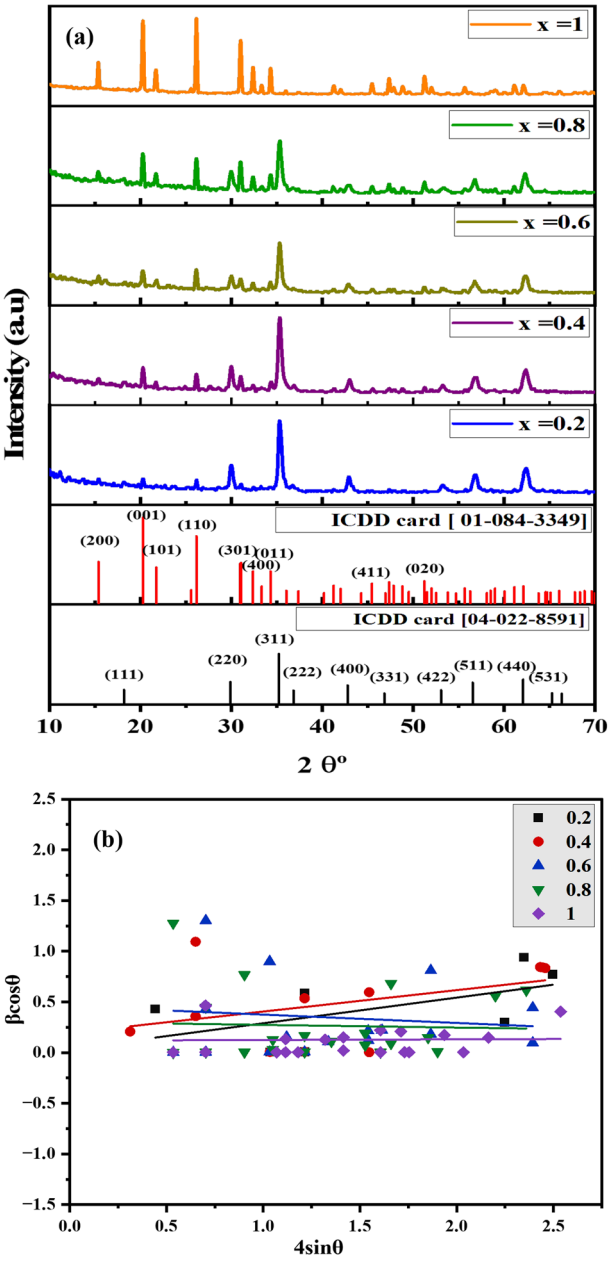

Fig. 1 **a** XRD pattern **b** *W–H* plot of nanocomposites of Mn-magnetite and V_2O_5 based on the formula of; $(V_2O_5)_x$. $(Mn_{0.4}(Fe_2O_4)_{2.4})_{(2-x)}$ $x = 0$, 0.2, 0.4, 0.6, 0.8, and 1

respectively. Even as the most significant peaks of the orthorhombic crystal structure, V_2O_5 [01-084-3349], were at $2\theta = 15.48°$, 21.82°, 26.25°, and 31.146°, which corresponded to (200), (101), (110), and (400), respectively. It was

observed that increasing V_2O_5 content resulted in a decrease in the peak intensity of $Mn_{0.4}Fe_{2.6}O_4$. The average crystallite size was calculated using Scherrer's equation [25]:

$$D = \frac{0.9}{\beta \cos} \tag{1}$$

where D is the Crystallite size, 0.9 symbolized the shape factor, λ is the wavelength of X-ray, β gives the full width at half maximum, and θ shows to the Bragg angle.

Using the Williamson–Hall (W–H) equation for peak broadening (β), which is given by the following relation: we were able to determine the lattice strains of $(V_2O_5)_x$. $(Mn_{0.4}Fe_{2.6}O_4)_{(2-x)}$, x = [0.2, 0.4, 0.6, 0.8 and 1].

$$\beta \cos\theta = 0.9\lambda/D + 4\varepsilon \sin\theta \tag{2}$$

where ε is the strain in the samples.

Figure 1b shows the W–H plot $(V_2O_5)_x$. $(Mn_{0.4}Fe_{2.6}O_4)_{(2-x)}$, where x = [0.2, 0.4, 0.6, 0.8, and 1]. The strain value (ε) which calculated using the slope of the fitted line [26] is listed in Table 1. The obtained micro-strain values show a decrease in value with increasing vanadium content. The composition's stoichiometry is shown by a lower micro-strain value, which promotes volumetric expansion [27].

In terms of the computed average crystallite size for $(V_2O_5)_x$. $(Mn_{0.4}Fe_{2.6}O_4)_{(2-x)}$, where x = [0.2, 0.4, 0.6, 0.8, and 1], the results demonstrate that the crystallite size decreases with increasing V_2O_5 content because of growing lattice distortion. With an increase in V_2O_5 contribution from 5.9 to 5.2 nm, the calculated crystallite size exhibits a decreasing behavior. Therefore, it appears that V_2O_5 has lower crystallinity than manganese-magnetite nanoparticles. Variations in preparation techniques are considered the cause of this tendency.

Morphology study

SEM and EDX

The morphological study of the composition of $(V_2O_5)_x$. $(Mn_{0.4}Fe_{2.6}O_4)_{(2-x)}$, where x = 0.2, 0.4, 0.5, 0.6, 0.8, and 1.0, was analyzed through SEM as shown in Fig. 2. At x = 0.2, pure vanadium oxide formed as fine agglomerated grains, while the

Table 1 Macrostrain and crystallite size of $(V_2O_5)_x$. $(Mn_{0.4}Fe_{2.6}O_4)_{(2-x)}$/PVDF composite, x = [0.2, 0.4, 0.6, 0.8, and 1]

Vanadium content	Strain (ε)	Crystallite size (nm)
0.2	0.25	5.9
0.4	0.21	7.2
0.6	−0.083	6.2
0.8	−0.027	52.7
1	0.006	17.6

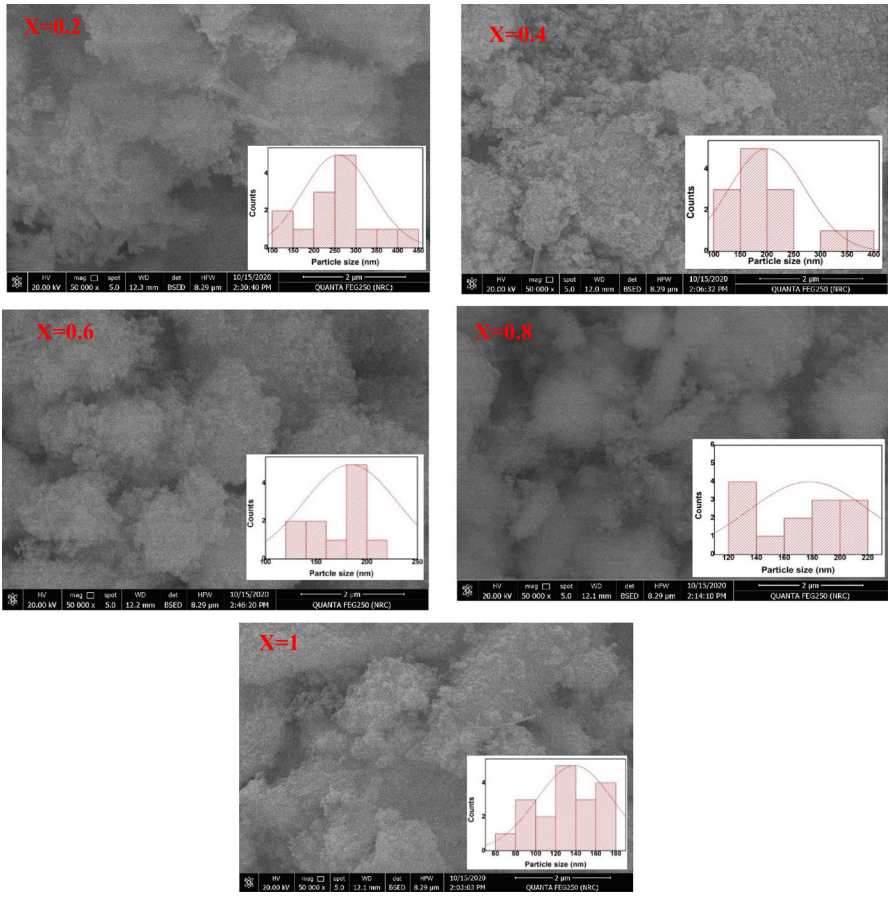

Fig. 2 SEM micrographs and histogram of $(V_2O_5)x$. $(Mn_{0.4}Fe_{2.6}O_4)_{(2-x)}$; $x = 0.2$, 0.4, 0.6, 0.8, and 1

composition at $x = 0.4$ tended to be formed of agglomerated grains with a fluffy surface. On the other hand, the composition of $x = 0.6$ has crumpled grains. Additionally, crystal grains with a composition of $x = 0.8$ have arbitrary orientations. The compositions of $x = 1.0$ are formed with a broad range of size distribution. Defects observed on the surface between vanadium oxide and manganese-doped magnetite are the main factors controlling the change in morphology. From the histogram of the prepared samples, we observed that the particle sizes decreased from 250 to 140 nm for $x = 0.2$ and $x = 1$, respectively. This is matched with results obtained from XRD.

The identification and confirmation of particular elements within the sample are achieved through the use of Energy-Dispersive X-ray Spectroscopy (EDX), thereby providing supplementary insights into the composition of $(V_2O_5)x$. $(Mn_{0.4}Fe_{2.6}O_4)_{(2-x)}$ is being studied for various values of x, specifically where $x = 0.2$, 0.4, 0.6, 0.8, and 1. The EDX spectrum for all ratios confirms,

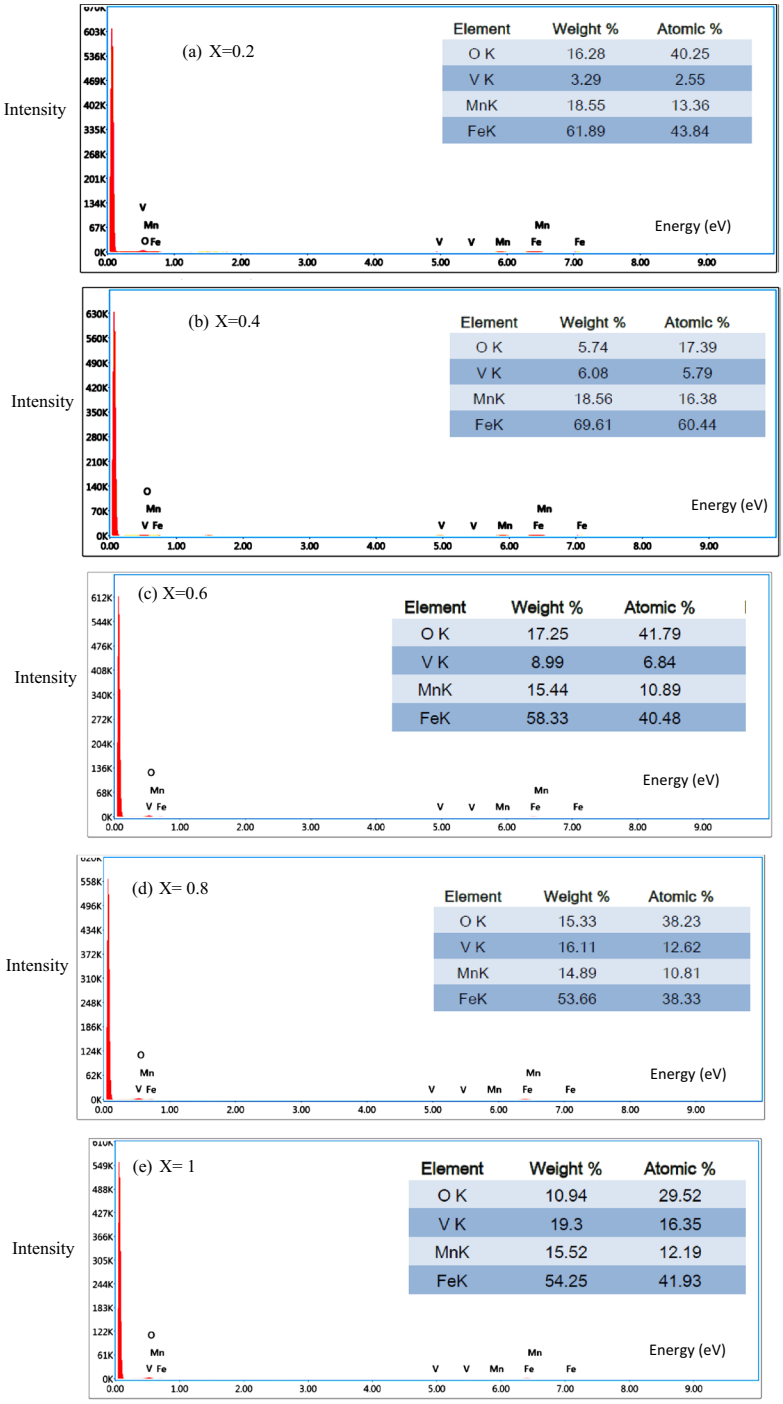

Fig. 3 **a–e** EDX micrographs of $(V_2O_5)x$. $(Mn_{0.4}Fe_{2.6}O_4)_{(2-x)}$; $x = 0.2$, 0.4, 0.6, 0.8, and 1

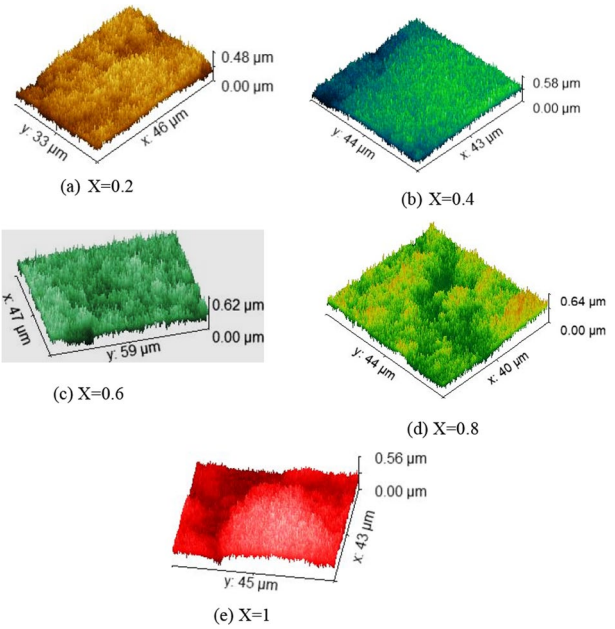

Fig. 4 **a–e** Surface roughness of $(V_2O_5)x.\ (Mn_{0.4}Fe_{2.6}O_4)_{(2-x)}$; $x = 0.2$, 0.4, 0.6, 0.8, and 1

Table 2 Surface roughness parameters of $(V_2O_5)x.\ (Mn_{0.4}Fe_{2.6}O_4)_{(2-x)}$; $x = 0.2$, 0.4, 0.6, 0.8, and 1 contain average roughness (R_a), roughness root mean square (R_q), surface area

x	R_a (nm)	R_q (nm)	Surface area (μm^2)
0.2	43.68	54.97	1512
0.4	55.69	69.76	2207
0.6	59.33	74.31	2235
0.8	59.74	74.45	2417
1	75.59	88.79	3563

as illustrated in Fig. 3a–e, that the composites consist of the elements Mn, O, Fe, and V. The qualitative yields, expressed in weight percent, are in excellent agreement with the specified stoichiometric ratios. Furthermore, the atomic ratios of Mn, V, Fe, and O ions in the different metals are within the targeted range. The observation was made that an increase in the ratios of V from $x = 0.2$ to $x = 1$ resulted in an increase in both its weight ratio (wt%) and atomic ratios (atomic%). This finding provides evidence for the presence of metal ions in $(V_2O_5)x.\ (Mn_{0.4}Fe_{2.6}O_4)_{(2-x)}$ nanocomposite was synthesized without the inclusion of any impurity ions.

Roughness study

The results presented in Fig. 4a–e, in conjunction with the data provided in Table 2, demonstrate that the roughness parameters, including Ra, Rq, and surface area, exhibited the lowest values for $x = 0.2$. The roughness parameters were somewhat higher for $x = 0.4$ and 0.6, while the highest value was observed for $x = 1$. Our findings suggest that there is a positive correlation between the content of V_2O_5 and the increase in surface area. The degree of crystallographic defects can be linked to surface roughness, resulting in elevated free energy and surface activity.

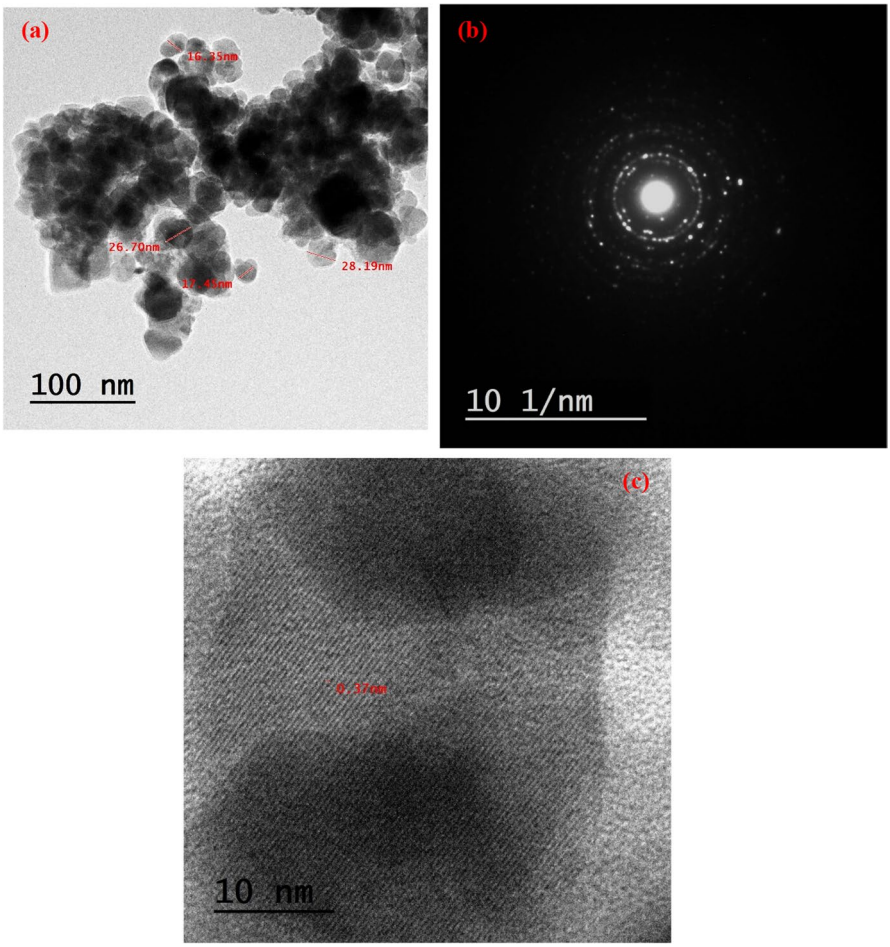

Fig. 5 **a** TEM, **b** SAED and **c** HRTEM inter-planar spacing of $(V_2O_5)_x$. $(Mn_{0.4}Fe_{2.6}O_4)_{(2-x)}$, $x = 0.2$

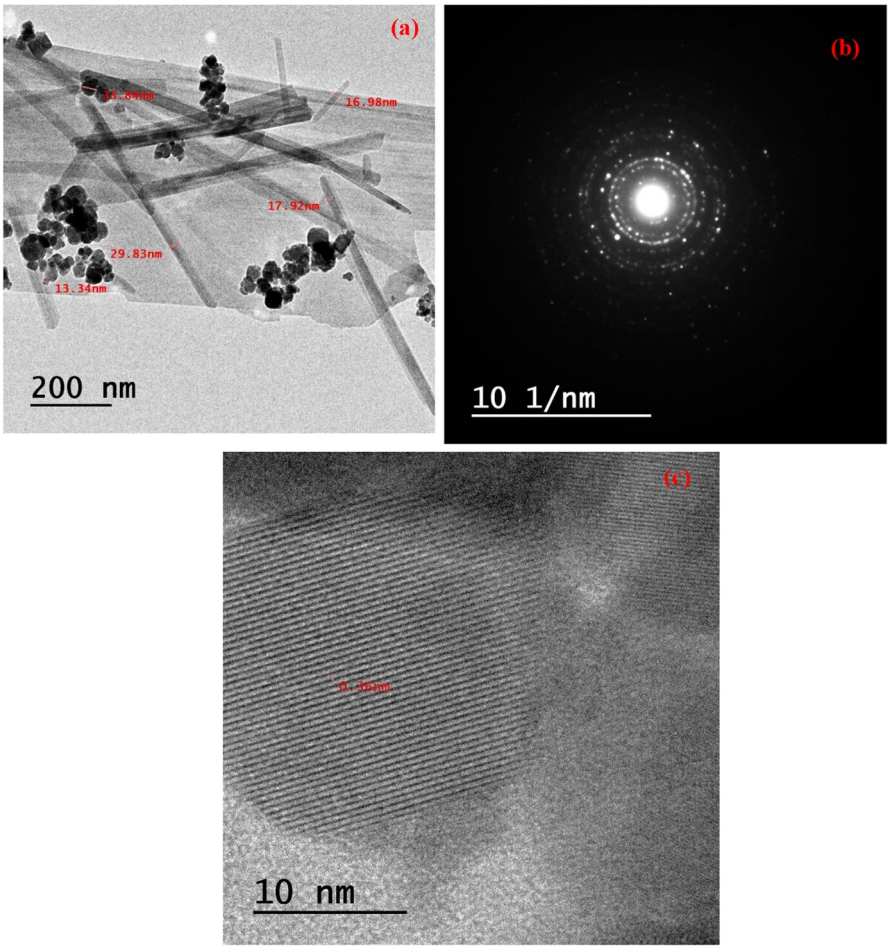

Fig. 6 **a** TEM, **b** SAED, and **c** HRTEM inter-planar spacing of $(V_2O_5)_{x.}$ $(Mn_{0.4}Fe_{2.6}O_4)_{(2-x)}$, $x=1$

HRTEM

Figures 5 and 6 show that the HRTEM analysis supports the formation of Mn-magnetite and V_2O_5 as dual phases that are related to the microstructure of $(V_2O_5)_{x.}$ $(Mn_{0.4}Fe_{2.6}O_4)_{(2-x)}$, where $x=0.2$ and 1. V_2O_5 seems to be shaped like a rod, whereas $Mn0.4Fe_{2.6}O_4$ appears to be shaped like microspheres. Figure 6a shows the mixed structure of V_2O_5 nanorods and microspheres $Mn_{0.4}Fe_{2.6}O_4$ of that forms a network. The agglomerated $Mn_{0.4}Fe_{2.6}O_4$ particles may cover the V_2O_5 nanorods in Fig. 5a because of the low ratio of V_2O_5 ($x=0.2$). The corresponding SAED image in Figs. 5b and 6b confirms the crystalline nature related to $(V_2O_5)_{x}$. $(Mn_{0.4}Fe_{2.6}O_4)_{(2-x)}$, $x=0.2$ and 1 microstructure. The inter-planar spacing of 0.37 and 0.36 nm in Figs. 5c and 6c, respectively, correspond to the (101) plane orthorhombic of V_2O_5, as discussed above in XRD analysis.

The HRTEM analysis presented in Figs. 5 and 6 provides evidence for the formation of Mn-magnetite and V_2O_5 as dual phases that are associated with the microstructure of $(V_2O_5)_x$. $(Mn_{0.4}Fe_{2.6}O_4)_{(2-x)}$, with x values of 0.2 and 1, exhibits distinct morphologies. V_2O_5 adopts a rod-like shape, while $Mn_{0.4}Fe_{2.6}O_4$ displays a microsphere morphology. The mixed structure of V_2O_5 nanorods and $Mn_{0.4}Fe_{2.6}O_4$ microspheres, which forms a network, is depicted in Fig. 6a. The particles of $Mn_{0.4}Fe_{2.6}O_4$ that have agglomerated might obscure the V_2O_5 nanorods depicted in Fig. 5a, which could be attributed to the relatively low ratio of V_2O_5 ($x=0.2$). The crystalline nature related to (V_2O_5) x is confirmed by the corresponding SAED image in

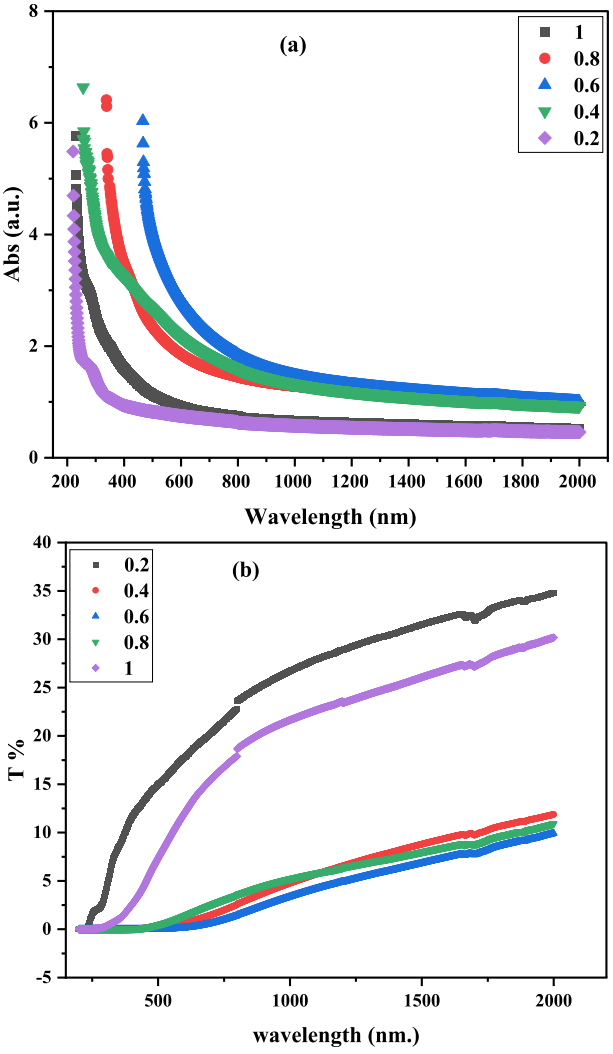

Fig. 7 **a**, **b** UV–NIR **a** absorption spectra and **b** transmittance % for $(V_2O_5)_x$. $(Mn_{0.4}Fe_{2.6}O_4)_{(2-x)}$/PVDF composite, $x=$[0.2, 0.4, 0.6, 0.8, and 1]

Figs. 5b and 6b. The microstructure of $(Mn_{0.4}Fe_{2.6}O_4)_{(2-x)}$, where x ranges from 0.2 to 1, is presented. The inter-planar spacing values of 0.37 nm and 0.36 nm observed in Figs. 5c and 6c, respectively, are consistent with the (101) plane orthorhombic crystal structure of V_2O_5, as previously discussed in the X-ray diffraction (XRD) analysis.

Optical properties

Figure 7a, b illustrates the absorbance and transmittance % of (UV-NIR) spectra for $(V_2O_5)_{x.}$ $(Mn_{0.4}Fe_{2.6}O_4)_{(2-x)}$,/PVDF composite, $x = [0.2, 0.4, 0.6, 0.8,$ and $1]$ in the range (200–2000 nm.). Figure 7a shows that the maximum absorption of the investigated samples shifted to the higher wavelength. The maximum wavelengths for sample $(V_2O_5)_{0.2}$ $(Mn0.4Fe_{2.6}O_4)_{1.8}$/PVDF composite range from 224 to 468 nm. By increasing the vanadium oxide concentration, the examined composites for sample $(V_2O_5)_{0.6}$ $(Mn_{0.4}Fe_{2.6}O_4)_{2.4}$/PVDF composite absorb light at shorter wavelengths. These values of spectrum absorption were got by combining vanadium oxide in various concentrations with the PVDF polymer, which absorbs light at 215 nm, $Mn_{0.4}F_{2.6}O_4$, which absorbs light at 315 nm, and the vanadium oxide [28].

Vanadium exists in different valence states: V^{3+}, V^{4+} and V^{5+}. Vanadium coordinates with oxygen to make distorted octahedral V^{3+}ions with corresponding three characteristic absorption bands at 350–400 nm, 580–680 nm, and a band at 200–400 nm attributed to electron transfer within the V^{3+} ions. These bands were observed in the present work in samples with concentrations [0.2, 0.4, and 1] of vanadium oxide.

The V^{5+} ion originates from the d° configuration and thus does not induce a d-d transition, but produces a characteristic charge transfer band at 380 nm [29, 30].

As the vanadium oxide content increases, a strong depolymerization occurs, producing its own network between vanadium atoms and the resulting oxygen atoms from the depolymerization process. And the number of V^{4+}–V^{4+} clusters increased due to the strong dipole–dipole interactions of network depolymerization and reorganization because of higher vanadium ion concentration [31]. By increasing the vanadium content ($x = 0.8$), the super-exchange interactions predominate among the resonance centers. The maximum absorption appears at 340 nm,

V^{3+} ions could exist as vanadyl ions $[VO^{2+}]$. At $x = 0.6$ of $(V_2O_5)_{x.}$ $(Mn_{0.4}Fe_{2.6}O_4)_{(2-x)}$,/PVDF composite, a band around 466 nm appears, which is attributed to tetravalent vanadium (VO^{2+}) ions.

Also, Fig. 7b shows that the smallest transmittance % (T%) corresponded to the sample $(V_2O_5)_{0.6}$ $(Mn_{0.4}(Fe_2O_4)_{2.4})_{0.4}$/PVDF composite.

The absorption coefficient (α) shows the amount of spectrum absorbed in the investigated samples. We calculated this using the absorbance (A) and the film thickness (d) by equation [32]:

$$\alpha = \frac{2.303A}{d} \tag{3}$$

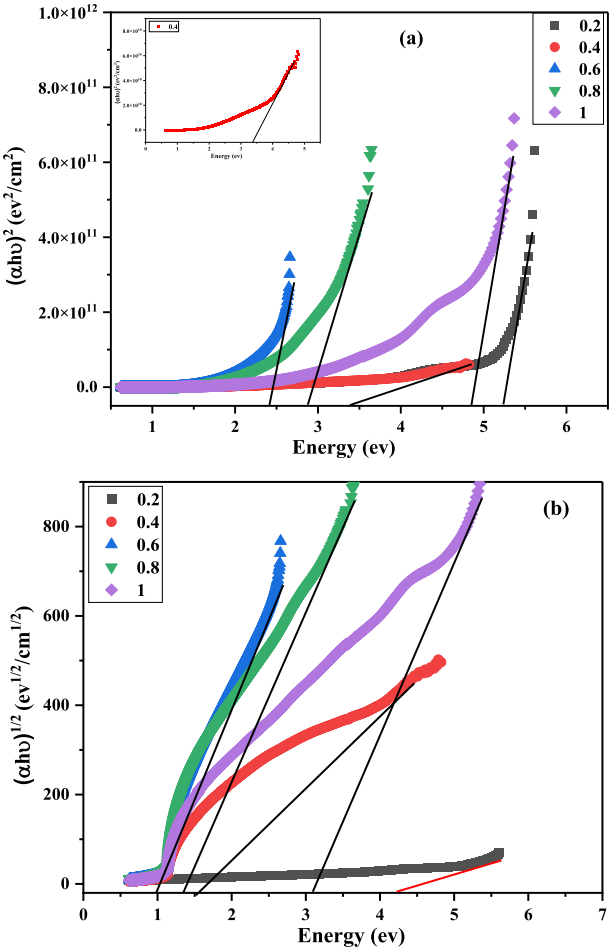

Fig. 8 **a**, **b**) Relation between photon energy and **a** $(\alpha h\nu)^2$ and **b** $(\alpha h\nu)^{1/2}$ for $(V_2O_5)_x$. $(Mn_{0.4}Fe_{2.6}O_4)_{(2-x)}$/PVDF composite, $x = [0.2, 0.4, 0.6, 0.8, \text{and } 1]$

Table 3 Direct and indirect bandgap energy of $(V_2O_5)_x$. $(Mn_{0.4}Fe_{2.6}O_4)_{(2-x)}$/PVDF composite, $x = [0.2, 0.4, 0.6, 0.8, \text{and } 1]$

Vanadium content	E_g^{Opt}(**dir**.) (ev)	E_g^{Opt}(**ind**.) (ev)
0.2	5.2	4.2
0.4	3.3	1.5
0.6	2.4	0.9
0.8	2.8	1.3
1	4.8	3

The optical direct bandgap E_g^{Opt}(**dir**.) and indirect band E_g^{Opt}(**ind**.) energies of the investigated samples were estimated by Tauc's relation [32, 33].

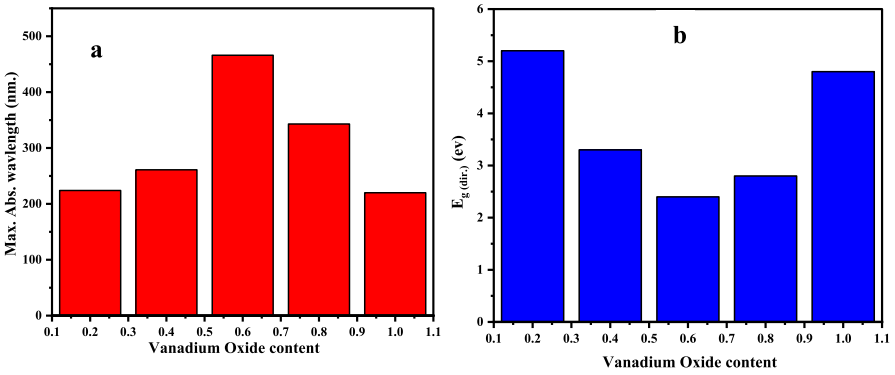

Fig. 9 **a**, **b** Variation of vanadium oxide content with maximum absorption wavelength, direct bandgap energy and indirect bandgap energy

$$(\alpha h\nu)^x = B(h\nu - E_g) \tag{4}$$

where B is constant, and $(h\nu)$ is the photon energy. for $x=2$ for direct bandgap and $x=½$, for indirect bandgap.

Figure 8a, b shows the relationship between photon energy and the estimation of direct bandgap energy, as well as the estimation of indirect bandgap energy in reverse. The obtained values are listed in Table 3. From the table and Fig. 8a, b it can be noted that $\boldsymbol{E_g^{Opt}}$**(dir.)** and $\boldsymbol{E_g^{Opt}}$**(ind.)** are decreased by increasing the vanadium oxide content until it reaches 0.6. After that they start to decrease again by increasing the vanadium oxide concentration Fig. 9. Where increasing the vanadium oxide content increases the electron transfer within V^{5+} itself and decreases the bandgap value. While the presence of tetravalent vanadyl (VO^{2+}) ions makes the movement of electric charge easier. Keeping the vanadium oxide content high makes the dipole–dipole interactions cancel each other out and gives rise to the bandgap energy.

Refractive index is one of the important optical characteristics. Depending on the material properties, the refractive index is essential in all optical instruments. Refractive index (n) can be obtained using the following equation [34]:

$$n = \frac{1}{T_s} + \left(\frac{1}{T_s} - 1\right) \tag{5}$$

where T_s is the maximum transmittance value.

Extinction coefficient K, real and imaginary parts of the dielectric constant ε_r and ε_i, and the optical conductivity $\boldsymbol{\sigma_{opt.}}$ were estimated by the following equations to be [32, 35, 36].

$$K = \frac{\alpha\lambda}{4\pi} \tag{6}$$

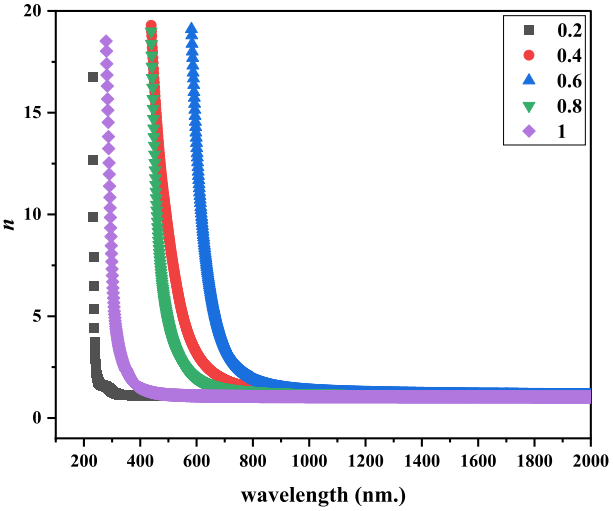

Fig. 10 Refractive index variation with wavelength for $(V_2O_5)_{x.}$ $(Mn_{0.4}Fe_{2.6}O_4)_{(2-x)}$/PVDF composite, $x = [0.2, 0.4, 0.6, 0.8, \text{and } 1]$

$$\varepsilon_r = n^2 - K^2 \tag{7}$$

$$\varepsilon_i = 2nK \tag{8}$$

$$\sigma_{opt.} = \frac{\alpha nc}{4\pi} \tag{9}$$

where c is the speed of light, and α is absorption coefficient.

Figure 10 illustrates the refractive index (n) of $(V_2O_5)_{x.}$ $(Mn_{0.4}Fe_{2.6}O_4)_{(2-x)}$/PVDF composite, where $x = [0.2, 0.4, 0.6, 0.8, \text{and } 1]$ was analyzed with wavelength. As the vanadium oxide content changes, the investigated samples exhibit a maximum

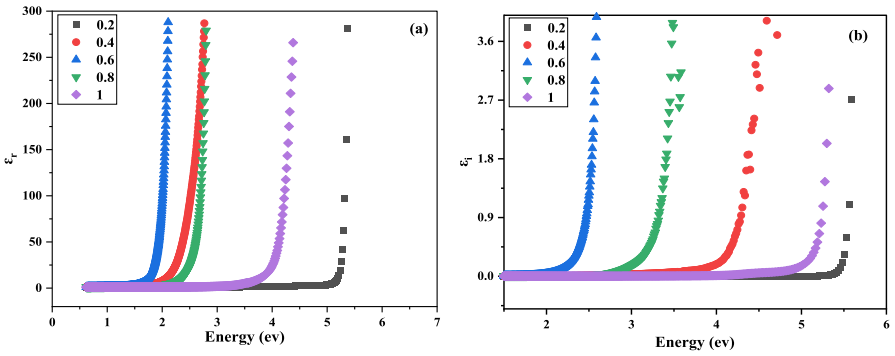

Fig. 11 **a**, **b** Relation between photon energy and **a** real ε_r and **b** and imaginary ε_i parts of dielectric constant and for $(V_2O_5)_{x.}$ $(Mn_{0.4}Fe_{2.6}O_4)_{(2-x)}$/PVDF composite, $x = [0.2, 0.4, 0.6, 0.8, \text{and } 1]$

value of (n) at different wavelengths in the spectrum. Where samples with vanadium content of 0.2 and 1 have their maximum values of (n) in the low range of wavelengths (200–400 nm), while samples with vanadium oxide content of 0.4, 0.6, and 0.8 have their maximum values of (n) in the visible range (450–800 nm).

Figure 11a, b shows the relation between ε_r, ε_i, and the incident photon energy. According to the figure, it is observed that a sample with 0.6 content of vanadium oxide has its maximum dielectric constant at extremely low energy [1.8 eV], while the sample with 0.2 content of vanadium oxide has its maximum dielectric constant at the highest energy [5.3 eV]. These results broaden the range of applications of the studied samples. The insulator-to-metal transition in vanadium oxide may be induced by thermal, electrical, optical, and mechanical stimuli. It is a reversible process with a hysteresis linked to vanadium oxide's electrical and optical characteristics [37, 38]. Consequently, vanadium oxide achieves maximal polarization at lower spectrum energy, where new energy levels are formed in the nanocomposite matrix. $\boldsymbol{\sigma}_{\mathbf{opt.}}$

As Fig. 12 shows, there is a variation in the optical conductivity $\boldsymbol{\sigma}_{\mathbf{opt.}}$ with the incident photon energy for the investigated samples with different vanadium oxide content. It is noted that the maximum $\boldsymbol{\sigma}_{\mathbf{opt.}}$ occurred at low energy in a sample with 0.6 vanadium oxide content, whereas high energy is required to transfer charges from the valence band to the conduction band in the sample with 0.2 vanadium oxide content.

Refractive index dispersion plays an important role in optoelectronic devices. In the present work, the Wemple–DiDomenico formula was used to study the refractive index dispersion of the investigated samples below the edge of the inter-band absorption, which depends on the photon energy.

The relationship between the refractive index and the photon energy was determined by [39, 40]:

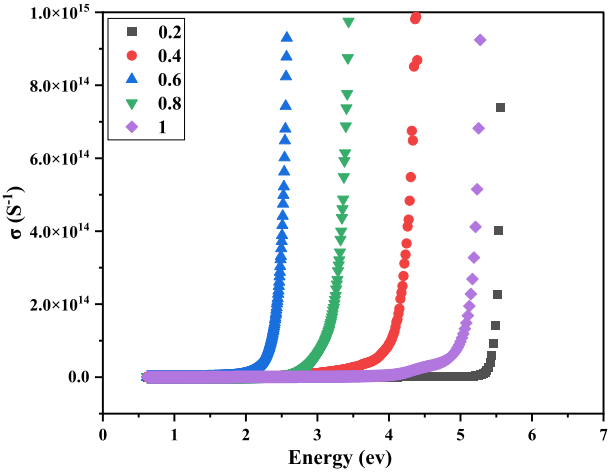

Fig. 12 Optical conductivity variation with wavelength for $(V_2O_5)_x$. $(Mn_{0.4}Fe_{2.6}O_4)_{(2-x)}$/PVDF composite, x = [0.2, 0.4, 0.6, 0.8, and 1]

Table 4 The single oscillator constants E_o and E_d, average oscillator strength S_o, inter-band oscillator wavelength λ_o, spectrum moments M_{-1} and M_{-3} of $(V_2O_5)_x$. $(Mn_{0.4}Fe_{2.6}O_4)_{(2-x)}$/PVDF, x = [0.2, 0.4, 0.6, 0.8 and 1] composite

Vanadium content	E_d (eV)	E_o (eV)	$S_0 \times 10^{-1}$ (m^{-2})	λ_0 (nm)	M_{-1}	M_{-3} $(eV)^{-2}$
0.2	2.14	30.0	1.9	5.5×10^{-1}	0.07	7.94×10^{-5}
0.4	5.09	14.6	2.23	8.7×10^{-1}	0.35	1.65×10^{-3}
0.6	6.50	13.4	2.60	9.1×10^{-1}	0.49	2.71×10^{-3}
0.8	6.73	18.3	3.04	8.1×10^{-1}	0.37	1.09×10^{-3}
1	2.48	28.1	1.93	5.9×10^{-1}	0.09	1.12×10^{-4}

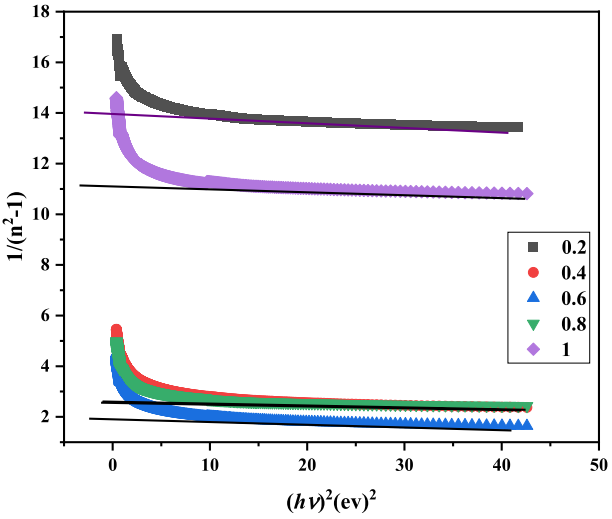

Fig. 13 Wemple–DiDomenico plot of $(V_2O_5)_x$. $(Mn_{0.4}Fe_{2.6}O_4)_{(2-x)}$/PVDF composite, x = [0.2, 0.4, 0.6, 0.8, and 1]

$$n^2 - 1 = \frac{E_o E_d}{[E_o^2 - (h\nu^2)]} \tag{10}$$

Through this relation and by fitting the linear part of the curves illustrated, the single oscillator constants E_o and E_d are calculated and listed in Table 4. We calculated these values from the slope and the intercept parts of the fitted lines of all investigated samples (Fig. 13).

Furthermore, the average oscillator strength S_o and the average inter-band oscillator wavelength λ_o were calculated using the following formula [36, 41].

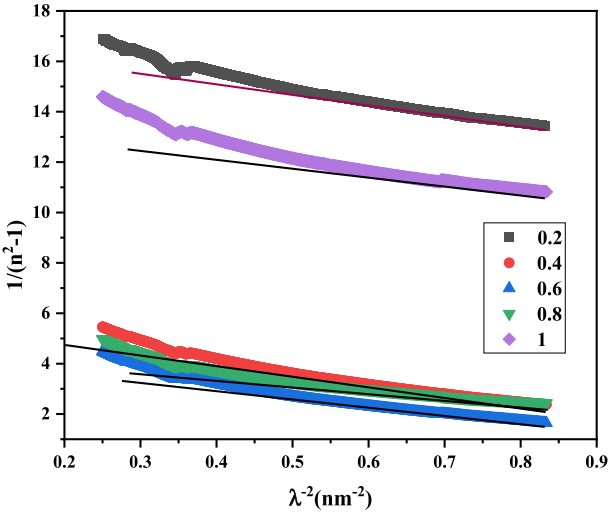

Fig. 14 Relationship between $\frac{1}{(n^2-1)}$ and λ^2 plot of $(V_2O_5)_x$. $(Mn_{0.4}Fe_{2.6}O_4)_{(2-x)}$/PVDF composite, $x=[0.2, 0.4, 0.6, 0.8, \text{and } 1]$

$$n^2 - 1 = \frac{S_o \lambda_o}{\left[1 - \left(\frac{\lambda_o}{\lambda}\right)^2\right]} \tag{11}$$

Figure 14 clarifies the relationship between $\frac{1}{(n^2-1)}$ and λ^2, from the slope and the intercept parts of the fitted lines of the plotted curves corresponding to the investigated samples So and λ_o, are calculated and listed in Table 4.

The effect of vanadium oxide on the moments M_{-1} and M_{-3} of the optical spectrum of $(V_2O_5)_x$. $(Mn_{0.4}Fe_{2.6}O_4)_{(2-x)}$/PVDF composite, $x=[0.2, 0.4, 0.6, 0.8 \text{ and } 1]$ are obtained by the following relations [42–44] and listed in Table 4.

$$E_o^2 = \frac{M_{-1}}{M_{-3}} \tag{12}$$

$$E_d^2 = \frac{M_{-1}^3}{M_{-3}} \tag{13}$$

From Table 4, we can conclude that the sample containing 0.6 of vanadium oxide has the lowest value of Eo and the largest λ_o, where E_o (average energy gap) decreases as the localized states increase and the transition occurs at low energy. While E_d (the oscillator strength) and S_o increased by increasing the manganese ferrite content, where E_d and S_o related to the structural rearrangement.

Small perturbations in physical systems close to equilibrium cause harmonic oscillations around the center of equilibrium. As the deviation from equilibrium is

large enough, most systems show unharmonic behavior creating new frequencies and a change in the oscillation period. The atomic valence electrons exhibit the same behavior when excited by an intense light beam. The response of the medium is described by the nonlinear polarization producing the field of nonlinear optics.

Materials exhibit a nonlinear optical response when they interact with an electric field of the order of interatomic fields (10^5–10^8 V/m). John Kerr studied the nonlinear optical response of solids and liquids subjected to strong external DC electric fields [50–54].

In such nonlinear medium, only one optical electromagnetic field is applied, the induced nonlinear polarization, P will effectively change the refractive index n_2 of the incident light beam. This is known as the optical Kerr effect [45, 46]. The values of susceptibilities can be estimated either classically by considering the harmonic and anharmonic movements of electrons on a minimal potential, or quantum mechanically by the theory of disturbances. The nonlinear behavior was studied using the following equations [47–49]:

$$P_{NL} = \chi^{(2)}E^2 + \chi^{(3)}E^3 \tag{14}$$

$$\chi^{(1)} = \frac{(n^2 - 1)}{4\pi} \tag{15}$$

$$\chi^{(3)} = \frac{\xi}{(4\pi)^2}\left(n_o^2 - 1\right)^4 \tag{16}$$

$$n_2 = \frac{12\pi\chi^{(3)}}{n_o} \tag{17}$$

where $\xi = 1.7 \times 10^{-10}$ (esu), $\boldsymbol{n_2}$, is the nonlinear refractive index, $\chi^{(3)}$ is the third order nonlinear optical susceptibility and $\chi^{(1)}$ the linear optical susceptibility [50, 51]. Figure 15a–c represents the plot of $\chi^{(1)}$, $\chi^{(3)}$ and $\boldsymbol{n_2}$ versus wavelength.

From the figure we can see that the investigated composites showed a remarkable nonlinear response in a wide range of wavelengths (200–1200). That is make $(V_2O_5)_x$. $(Mn_{0.4}Fe_{2.6}O_4)_{(2-x)}$/PVDF, $x = [0.2, 0.4, 0.6, 0.8$ and $1]$ composites have a wide range of applications in optoelectronics.

Contact angle and wettability

The wettability of $(V_2O_5)_x$ $(Mn_{0.4}Fe_{2.6}O_4)_{(2-x)}$/PVDF, where $x = [0.2, 0.4, 0.6, 0.8,$ and $1]$ composites is being investigated using contact angle analysis. The water contact angle values of the PVDF film range from 85° to 130°, as reported in published works, which cause the hydrophilic behavior of PVDF films [52, 53]. The hydrophobicity of PVDF films originates from their fluorinated composition [52, 53]. The hydrophobicity of PVDF films originates from their fluorinated composition [54–56]. Contact angles of the investigated samples are shown in Fig. 16 and listed in Table 5. The figure and table show that the contact angle decreases

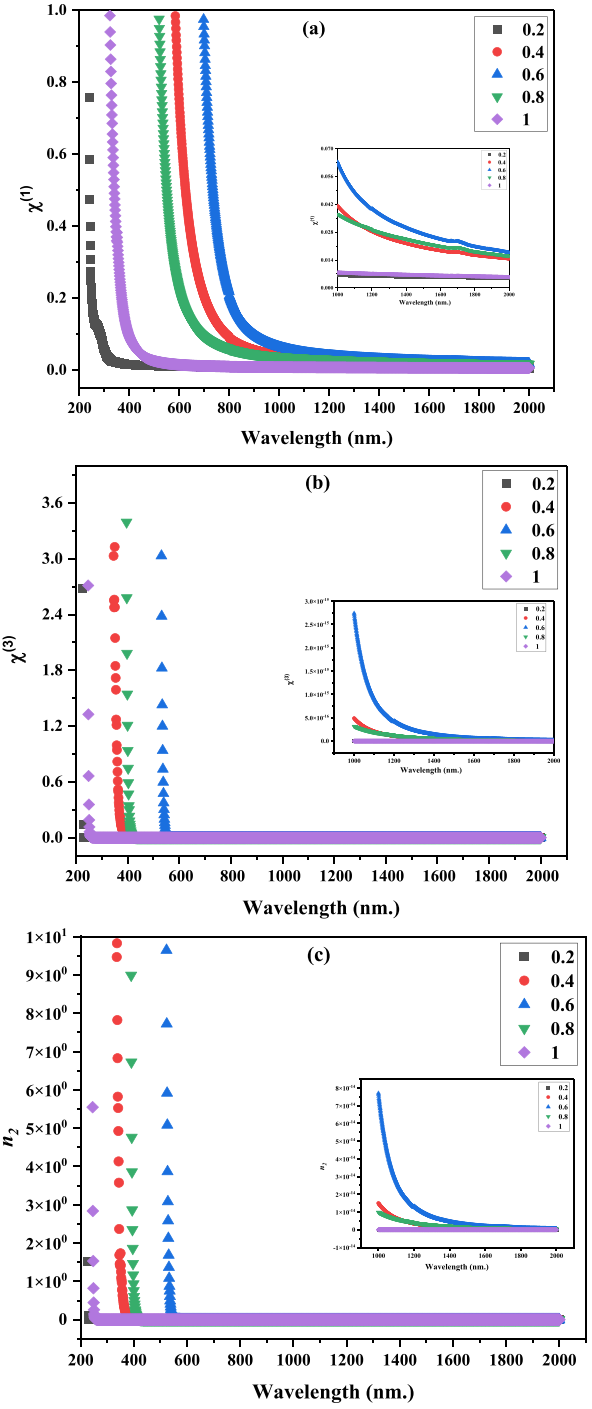

Fig. 15 **a** $\chi^{(1)}$, **b** $\chi^{(3)}$ and **c** n_2 verses wavelength of $(V_2O_5)_x$.$(Mn_{0.4}Fe_{2.6}O_4)_{(2-x)}$/PVDF composite, x = [0.2, 0.4, 0.6, 0.8, and 1]

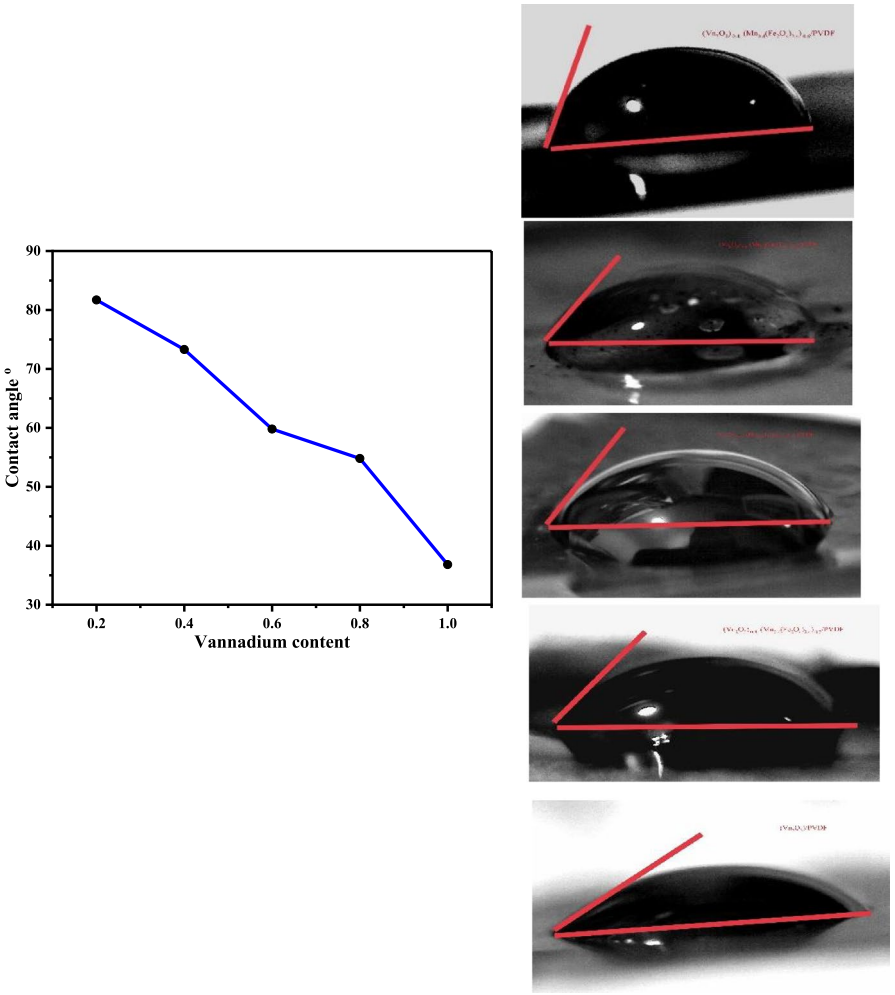

Fig. 16 Contact angle of $(V_2O_5)_x$. $(Mn_{0.4}Fe_{2.6}O_4)_{(2-x)}$/PVDF composite, $x = [0.2, 0.4, 0.6, 0.8, \text{and } 1]$

Table 5 The contact angle of $(V_2O_5)_x$. $(Mn_{0.4}Fe_{2.6}O_{4)(2-x)}$/PVDF, $x = [0.2, 0.4, 0.6, 0.8 \text{ and } 1]$ composite

Vanadium content	Contactangle(degree)
0.2	81.7
0.4	73.3
0.6	66
0.8	59.8
1	54.8

with an increase in vanadium oxide content. The decrease in the contact angle value by increasing the vanadium oxide content indicates an increased tendency of PVDF to be hydrophilic [57]. This decrease could be due to the increase in surface area and roughness, as well as the interconnected pore morphology produced by increasing the vanadium oxide content [58], which causes the absorption of water. These results support the use of $(V_2O_5)x$. $(Mn_{0.4}Fe_{2.6}O_4)(2-x)$/PVDF composite is an efficacious membrane in different applications, such as the removal of pollutants, bio-ethanol recovery, and as a lithium-ion battery separator [59].

Conclusion

The present study focuses on the investigation of nanocomposites comprising varying proportions of V_2O_5, and manganese magnetite. The crystal structure was analyzed using X-ray diffraction (XRD) technique. The results indicated that an increase in V_2O_5 content resulted in a reduction in the peak intensity of $Mn_{0.4}Fe_{2.6}O_4$. Additionally, the calculated crystallite size decreased from 79 to 50 nm. The particle size distribution, as determined by the histogram of the same ratios, also decreased from 250 to 140 nm. The analysis of the surface structure revealed that the morphology underwent significant alterations in response to variations in composition. The alteration in morphology can be attributed to the surface defects between vanadium oxide and manganese-doped magnetite. The present study reveals that the direct and indirect energy bandgaps of the samples prepared exhibit a decreasing trend with an increase in the concentration of vanadium oxide until it reaches 0.6. However, a further increase in the concentration of vanadium oxide leads to an increase in the energy bandgap values. The findings of our study indicate that the dielectric constant of the sample containing 0.6 content of vanadium oxide exhibits its highest value at an extremely low energy of 1.8 eV. Conversely, the sample with 0.2 content of vanadium oxide demonstrates its maximum dielectric constant at the highest energy [5.3 eV]. These findings broaden the scope of potential applications for the samples under investigation.

The incorporation of $(V_2O_5)_x$ Nanocomposites of $(Mn_{0.4}Fe_{2.6}O_4)_{(2-x),}$ where x ranges from 0.2 to 1, when combined with PVDF polymers, has been found to enhance the hydrophilicity of PVDF films. The nanocomposite under investigation exhibits promising characteristics for optoelectronic applications, including low cost, long-lasting durability, and high performance. Additionally, it serves as an elastic polymer membrane with adjustable lenses, further expanding its potential applications.

Author contributions MME-M contributed to conceptualization, methodology, formal analysis, data curation, investigation, writing, and review. MKA contributed to conceptualization, methodology, formal analysis, and data curation. RR contributed to conceptualization, methodology, formal analysis, investigation, data curation, visualization, writing, and review.

Funding Open access funding provided by The Science, Technology & Innovation Funding Authority (STDF) in cooperation with The Egyptian Knowledge Bank (EKB).

Declarations

Conflict of interest The authors declare that they have no conflict of interests.

References

1. Zhang Y, Jiang H, Wang Q et al (2018) Kelp-derived three-dimensional hierarchical porous N, O-doped carbon for flexible solid-state symmetrical supercapacitors with excellent performance. Appl Surf Sci. https://doi.org/10.1016/j.apsusc.2018.04.061
2. Ramadan R, El-Masry MM (2021) Comparative study between CeO_2/Zno and CeO_2/SiO_2 nanocomposites for (Cr^{6+}) heavy metal removal. Appl Phys A Mater Sci Process. https://doi.org/10.1007/s00339-021-05037-z
3. Huang T, Yu J, Han J et al (2015) Oxygen reduction catalytic characteristics of vanadium carbide and nitrogen doped vanadium carbide. J Power Sources. https://doi.org/10.1016/j.jpowsour.2015.09.104
4. Światowska-Mrowiecka J, Maurice V, Zanna S et al (2007) XPS study of Li ion intercalation in V_2O_5 thin films prepared by thermal oxidation of vanadium metal. Electrochim Acta. https://doi.org/10.1016/j.electacta.2006.12.050
5. Ramadan R, Ismail AM (2022) Tunning the physical properties of PVDF/PVC/zinc ferrite nanocomposites films for more efficient adsorption of Cd(II). J Inorg Organomet Polym Mater. https://doi.org/10.1007/s10904-021-02176-x
6. El-Masry MM, Mahmoud AE, Morshidy HY, Ramadan R (2023) Cu^{2+}- and Zn^{2+}-doped cobalt spinel ferrite: insights on structural, thermal conduction, electric, magnetic and elastic properties. J Mater Sci Mater Electron 34:383. https://doi.org/10.1007/s10854-022-09777-3
7. El-Masry MM, Imam NG (2022) A comparative study between Ag–CuO/epoxy and Mg–CuO/epoxy hybrid nanocomposites: impressive electrical, mechanical and thermal properties. J Mater Res Technol. https://doi.org/10.1016/j.jmrt.2022.03.039
8. El-Masry MM, Ramadan R (2022) The effect of $CoFe_2O_4$, $CuFe_2O_4$ and Cu/$CoFe_2O_4$ nanoparticles on the optical properties and piezoelectric response of the PVDF polymer. Appl Phys A Mater Sci Process. https://doi.org/10.1007/s00339-021-05238-6
9. Li M, Sun G, Yin P et al (2013) Controlling the formation of rodlike V_2O_5 nanocrystals on reduced graphene oxide for high-performance supercapacitors. ACS Appl Mater Interfaces. https://doi.org/10.1021/am403739g
10. Heiba ZK, Mohamed MB, Wahba AM, Almalowi MI (2018) Effect of vanadium doping on structural and magnetic properties of defective nano-nickel ferrite. Appl Phys A Mater Sci Process. https://doi.org/10.1007/s00339-018-1721-3
11. El-naggar AM, Mohamed MB, Aldhafiri AM, Heiba ZK (2020) Effect of vacancies and vanadium doping on the structural and magnetic properties of nano $LiFe_{2.5}O_4$. J Mater Res Technol. https://doi.org/10.1016/j.jmrt.2020.11.097
12. Lebourgeois R, Duguey S, Ganne JP, Heintz JM (2007) Influence of V_2O_5 on the magnetic properties of nickel-zinc-copper ferrites. J Magn Magn Mater. https://doi.org/10.1016/j.jmmm.2006.10.698

13. Ahmad MW, Anand S, Dey B et al (2022) Asymmetric supercapacitors based on porous $MnMoS_4$ nanosheets-anchored carbon nanofiber and N, S-doped carbon nanofiber electrodes. J Alloys Compd. https://doi.org/10.1016/j.jallcom.2022.164271
14. Heiba ZK, Mohamed MB, El-naggar AM et al (2021) Impact of ZnCdS/M (M = Co, Fe, Mn, V) doping on the structure and optical properties of PVA/PVP polymer. J Polym Res 36:56. https://doi.org/10.1007/s10965-021-02840-3
15. Rajesh K, Crasta V, Rithin Kumar NB et al (2019) Structural, optical, mechanical and dielectric properties of titanium dioxide doped PVA/PVP nanocomposite. J Polym Res. https://doi.org/10.1007/s10965-019-1762-0
16. Caseri W (2009) Inorganic nanoparticles as optically effective additives for polymers. Chem Eng Commun. https://doi.org/10.1080/00986440802483954
17. Ghazali N, Basirun WJ, Nor AM, Johan MR (2020) Super-amphiphobic coating system incorporating functionalized nano-Al_2O_3 in polyvinylidene fluoride (PVDF) with enhanced corrosion resistance. Coatings. https://doi.org/10.3390/coatings10040387
18. Indolia AP, Gaur MS (2013) Optical properties of solution grown PVDF–ZnO nanocomposite thin films. J Polym Res. https://doi.org/10.1007/s10965-012-0043-y
19. Shaltout AA, Mostafa NY, Mahani RM et al (2020) Investigation of structural and optical properties of molybdenum disulfide flakes/polyvinylidene fluoride nanocomposites. J Mater Res Technol. https://doi.org/10.1016/j.jmrt.2020.10.009
20. Ribeiro S, Meira RM, Correia DM et al (2020) Silica nanoparticles surface charge modulation of the electroactive phase content and physical-chemical properties of poly(vinylidene fluoride) nanocomposites. Compos B Eng. https://doi.org/10.1016/j.compositesb.2020.107786
21. Gaabour LH (2020) Analysis of spectroscopic, optical and magnetic behaviour of PVDF/PMMA blend embedded by magnetite (Fe_3O_4) nanoparticles. Opt Photonics J. https://doi.org/10.4236/opj.2020.108021
22. Hafez RS, Ramadan R, El-Khiyami SS (2021) Investigation of structural, optical, magnetic, and electrical properties of PMMA doped with magnetite nanoparticles. J Mater Sci Mater Electron. https://doi.org/10.1007/s10854-021-06015-0
23. El-Masry MM, Ramadan R (2022) Enhancing the properties of PVDF/MFe_2O_4; (M: Co–Zn and Cu–Zn) nanocomposite for the piezoelectric optronic applications. J Mater Sci Mater Electron 33:15946–15963. https://doi.org/10.1007/s10854-022-08493-2
24. D D, Mark JAM, Raghavan T, Jesuraj JP (2021) Fabrication of $MnFe_2O_4$ and Ni: $MnFe_2O_4$ nanoparticles for ammonia gas sensor application. Inorg Chem Commun. https://doi.org/10.1016/j.inoche.2020.108355
25. Arman MM, Ahmed MK, El-Masry MM (2023) Cellulose acetate polymer spectroscopic study comprised $LaFeO_3$ perovskite and graphene as a UV-to-visible light converter used in several applications. J Mol Struct 1281:135153. https://doi.org/10.1016/j.molstruc.2023.135153
26. Kibasomba PM, Dhlamini S, Maaza M et al (2018) Strain and grain size of TiO_2 nanoparticles from TEM, Raman spectroscopy and XRD: the revisiting of the Williamson–Hall plot method. Results Phys. https://doi.org/10.1016/j.rinp.2018.03.008
27. Dhanasekaran V, Mahalingam T, Chandramohan R (2013) Post heat treatment effect on electrochemically synthesized CuO thin films. ECS Trans. https://doi.org/10.1149/04524.0073ecst
28. Kaspar P, Sobola D, Částková K et al (2020) Characterization of polyvinylidene fluoride (PVDF) electrospun fibers doped by carbon flakes. Polymers (Basel). https://doi.org/10.3390/polym12122766
29. Mehdikhani B, Mirhadi B (2012) Effect of V_2O_5 additions on the crystallisation of sodium silicate glasses. Glass Technol Eur J Glass Sci Technol Part A 53:146
30. Abdelaziz TD, Ezzeldin FM, el Batal HA, Abdelghany AM (2014) Optical and FT Infrared spectral studies of vanadium ions in cadmium borate glass and effects of gamma irradiation. Spectrochim Acta A Mol Biomol Spectrosc. https://doi.org/10.1016/j.saa.2014.04.035
31. Vedeanu N, Cozar O, Stanescu R et al (2013) Structural investigation of new vanadium-bismuth-phosphate glasses by IR and ESR spectroscopy. J Mol Struct 1044:323
32. El-Masry MM, Ibrahim AS (2022) Ag-CuO/rGO/PVDF nanocomposite synthesized via simple method as a broadband non-linear optical material for optronic applications. J Mater Sci Mater Electron. https://doi.org/10.1007/s10854-022-08066-3
33. Kayani ZN, Aslam H (2021) Investigation of structural, optical, antibacterial, and dielectric properties of V-doped copper oxide thin films: Comparison with undoped copper oxide thin films. Adv Powder Technol. https://doi.org/10.1016/j.apt.2021.05.026

34. Ramírez-Malo JB, Márquez E, Villares P, Jiménez-Garay R (1992) Determination of the refractive index and optical absorption coefficient of vapor-deposited amorphous As–S films from transmittance measurements. Phys Status Solidi A. https://doi.org/10.1002/pssa.2211330234
35. Hassanien AS, Sharma I (2019) Band-gap engineering, conduction and valence band positions of thermally evaporated amorphous Ge_{15-x} Sb_x Se_{50} 35 thin films: influences of Sb upon some optical characterizations and physical parameters. J Alloys Compd. https://doi.org/10.1016/j.jallcom.2019.05.252
36. Bakry AM, El-Korashy A (2010) Thickness effect on the optical parameters of Ge–Se–Te films. Egypt J Solids. https://doi.org/10.21608/ejs.2010.148691
37. Hashemi MRM, Berry CW, Merced E et al (2014) Direct measurement of vanadium dioxide dielectric properties in w-band. J Infrared Millim Terahertz Waves. https://doi.org/10.1007/s10762-014-0065-0
38. Abdul-Ameer NM, Khaleel IH, Hasan SQA, Abdulrid MC (2021) The effect of temperature width on dielectric constant of vanadium dioxide. In: Key engineering materials
39. Aftab M, Butt MZ, Ali D et al (2021) Optical and electrical properties of NiO and Cu-doped NiO thin films synthesized by spray pyrolysis. Opt Mater (Amst). https://doi.org/10.1016/j.optmat.2021.111369
40. Ezealigo BN, Nwanya AC, Ezugwu S et al (2020) Method to control the optical properties: band gap energy of mixed halide organolead perovskites. Arab J Chem. https://doi.org/10.1016/j.arabjc.2017.09.002
41. Abd-Elnaiem AM, Abdelraheem AM, Abdel-Rahim MA, Moustafa S (2022) Substituting silver for tellurium in selenium–tellurium thin films for improving the optical characteristics. J Inorg Organomet Polym Mater. https://doi.org/10.1007/s10904-022-02250-y
42. Bakr NA, Jandow NN, Habubi NF (2014) Optical and dispersion parameters of ZnS thin films prepared by flash evaporation method. Int Lett Chem Phys Astron. https://doi.org/10.18052/www.scipress.com/ilcpa.39.52
43. Bouarissa A, Gueddim A, Bouarissa N, Maghraoui-Meherzi H (2020) Optical response and magnetic moment of MoS_2 material. Optik (Stuttg). https://doi.org/10.1016/j.ijleo.2019.164080
44. Jin C, Kim J, Wu K et al (2017) On optical dipole moment and radiative recombination lifetime of excitons in WSe_2. Adv Funct Mater. https://doi.org/10.1002/adfm.201601741
45. Miyagawa K, Nagai M, Ashida M et al (2021) Enhanced magneto-optical Kerr effect of GaAs-Based *P–N* junctions in the terahertz range. J Infrared Millim Terahertz Waves. https://doi.org/10.1007/s10762-021-00779-6
46. Choi GM (2018) Magneto-optical Kerr effect driven by spin accumulation on Cu, Au, and Pt. Appl Sci (Switz). https://doi.org/10.3390/app8081378
47. Abazari R, Yazdani E, Nadafan M et al (2021) Third-order nonlinear optical behavior of an amide-tricarboxylate zinc(II) metal-organic framework with two-fold 3D+3D interpenetration. Inorg Chem. https://doi.org/10.1021/acs.inorgchem.1c00997
48. Kumar P, Mathpal MC, Hamad S et al (2019) Cu nanoclusters in ion exchanged soda-lime glass: study of SPR and nonlinear optical behavior for photonics. Appl Mater Today. https://doi.org/10.1016/j.apmt.2019.02.016
49. Inwati GK, Kumar P, Singh M et al (2021) Study of photoluminescence and nonlinear optical behaviour of AgCu nanoparticles for nanophotonics. Nano-Struct Nano-Objects. https://doi.org/10.1016/j.nanoso.2021.100807
50. Parra I, Valbuena S, Racedo F (2021) Measurement of non-linear optical properties in graphene oxide using the Z-scan technique. Spectrochim Acta A Mol Biomol Spectrosc. https://doi.org/10.1016/j.saa.2020.118833
51. Tichá H, Tichý L (2002) Semiempirical relation between non-linear susceptibility (refractive index), linear refractive index and optical gap and its application to amorphous chalcogenides. J Optoelectron Adv Mater 4:381
52. Kitabata M, Taddese T, Okazaki S (2018) Molecular dynamics study on wettability of poly(vinylidene fluoride) crystalline and amorphous surfaces. Langmuir. https://doi.org/10.1021/acs.langmuir.8b02286
53. Zhang J, Huang X, Shi J et al (2021) A visual bi-layer indicator based on roselle anthocyanins with high hydrophobic property for monitoring griskin freshness. Food Chem. https://doi.org/10.1016/j.foodchem.2021.129573
54. Dey R, Hussain S, Pal AK (2020) Inducing hydrophobicity in cellulose by using polyvinylidene difluoride (PVDF) to produce freestanding cellulose/PVDF composite films. Cellul Chem Technol. https://doi.org/10.35812/CelluloseChemTechnol.2020.54.77

55. Folgado E, Guerre M, Bijani C et al (2016) Well-defined poly(vinylidene fluoride) (PVDF) based-dendrimers synthesized by click chemistry: enhanced crystallinity of PVDF and increased hydrophobicity of PVDF films. Polym Chem. https://doi.org/10.1039/c6py01167e
56. Moradi R, Karimi-Sabet J, Shariaty-Niassar M, Koochaki MA (2015) Preparation and characterization of polyvinylidene fluoride/graphene superhydrophobic fibrous films. Polymers (Basel). https://doi.org/10.3390/polym7081444
57. Huang SI, Chen H (2011) Study on the improvement of hydrophobicity of PVDF films. J Thermoplast Compos Mater. https://doi.org/10.1177/0892705709358504
58. Cao J, Zhang H, Xu W, Li X (2014) Poly(vinylidene fluoride) porous membranes precipitated in water/ethanol dual-coagulation bath: The relationship between morphology and performance in vanadium flow battery. J Power Sources. https://doi.org/10.1016/j.jpowsour.2013.10.069
59. Ahmadian A (2019) Design and fabrication of high-capacity lithium-ion batteries using electro- spun graphene modified vanadium pentoxide cathodes. Purdue University Graduate School. Thesis. https://doi.org/10.25394/PGS.9037004.v1

Authors and Affiliations

Rania Ramadan[1] · M. K. Ahmed[2,3] · Mai M. El-Masry[4]

✉ Rania Ramadan
rramadan@sci.cu.edu.eg

✉ Mai M. El-Masry
mai.elmasry@thebes.edu.eg

[1] Materials Science Lab (1), Physics Department, Faculty of Science, Cairo University, Giza, Egypt

[2] Faculty of Nanotechnology for Postgraduate Studies, Cairo University, El-Sheikh Zayed, Egypt

[3] Department of Physics, Faculty of Science, Suez University, Suez 43518, Egypt

[4] Basic Science Department, Higher Engineering Institute, Thebes Academy, Cairo, Egypt